Research Article

Unsteady pressure measurement and numerical simulations in an end-wall region of a linear blade cascade

Erik Flídr[1] · Petr Straka[1] · Milan Kladrubský[1] · Tomáš Jelínek[1]

Received: 31 July 2020 / Accepted: 5 July 2021
Published online: 31 July 2021

Abstract

This contribution describes experimental and numerical research of an unsteady behaviour of a flow in an end-wall region of a linear nozzle cascade. Effects of compressibility ($M_{2,is}$) and inlet flow angle (α_1) were investigated. Reynolds number ($Re_{2,is} = 8.5 \times 10^5$) was held constant for all tested cases. Unsteady pressure measurement was performed at the blade mid-span in the identical position $\mathfrak{s}$ to obtain reference data. Surface flow visualizations were performed as well as the steady pressure measurement to support conclusions obtained from the unsteady measurements. Comparison of the surface Mach number distributions obtained from the experiments and from the numerical simulations are presented. Flow visualizations are then compared with calculated limiting streamlines on the blade suction surface. It was shown, that the flow structures in the end-wall region were not affected by the primary flow at the blade mid-span, even when the shock wave formed. This conclusion was made from the experimental, numerical, steady as well as unsteady points of view. Three significant frequencies in the power spectra suggested that there was a periodical interaction between the vortex structures in the end-wall region. Based on the data analyses, anisotropic turbulence was observed in the cascade.

Article Highlights

- Periodicflow behaviour was found in the near-wall region.
- Complicatedflow structures occur in the position where the shock wave inter-acted with the near-wallflow.
- In house numerical model can predict theflow properties with accuracy de-scribed in the paper.

Keywords Linear blade cascade · Unsteady pressure measurement · Numerical simulations · Secondary flow

List of symbols

Latin

a, b	Variables in Eq. (5)
c	Blade chord
E	Voltage
f	Frequency
h	Blade height
$\mathcal{K}$	transducer constant
M	Mach number
p	Pressure
r	Gas constant
Re	Reynolds number
s	Surface coordinate
t	Pitch
T	Thermodynamic temperature
u	Velocity
$\mathcal{U}$	Velocity ratio
x, y, z	Cartesian coordinates
$\mathfrak{s}$	Separation line
$\mathfrak{S}$	Separation point

✉ Erik Flídr, flidr@vzlu.cz | [1]VZLU - Beranových 130, 199 05 Prague - Letňany, Czech Republic.

$\mathfrak{r}$	Reattachment line
$\mathfrak{R}$	Reattachment point

Greek

α	Flow angle
β	Exponent in eq. (3)
δ	Exponent for PSD
κ	Ratio of specific heats
Π	Pressure ratio
σ^2	Variance
τ	Time

Index

1	Cascade inlet
2	Cascade outlet
is	Isentropic
lp	Low pass
ms	Mid-span
nw	Near-wall
own	Own frequency
sampl	Sampling
STD	Standard deviation

Abbreviations

FS	Full scale
RDG	Reading

1 Introduction

1.1 Secondary flow

Secondary flow within blade cascades is a complicated flow phenomenon. It is a highly three-dimensional flow, where interactions between several vortices occur. Effects of many parameters (inlet flow angle [1, 2], compressibility [3], viscosity [4], turbulence intensity [5], thickness of the inlet boundary layer [6, 7], etc.) on secondary flow within a cascade were experimentally investigated. Results of these works were used for the formulation of several types of secondary flow models beginning from the simplest (Langston [8]) to the most advanced and complex(Wang et al. [9]).

Comprehensive reviews about the secondary flow were written by Sieverding [10], Langston [11] and Ligrani [12].

Based on the literature cited above, the end-wall flow evolution can be briefly described in the following manner. The separated inlet boundary layer in front of the cascade rolls up into the horse-shoe vortex (HSV) due to the conservation of mass and momentum, see Fig. 1. The suction leg of the HSV moves along the suction surface of the blade, while the pressure leg of the HSV is drawn into the blade passage due to the pressure gradient. This leg consumes the low-momentum fluid from the end-wall

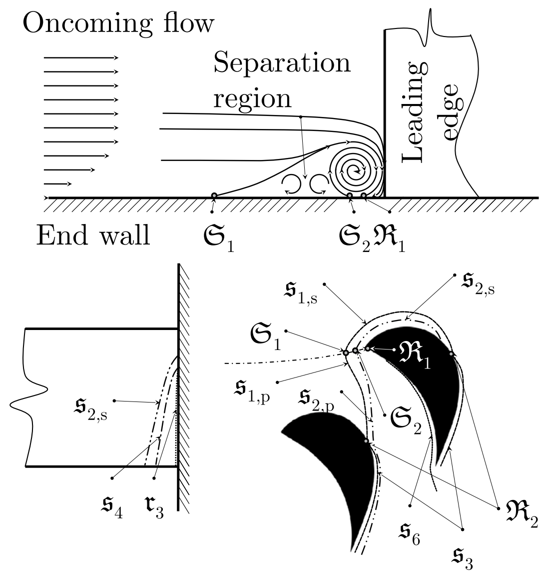

Fig. 1 System of the separation and reattachment points ($\mathfrak{S}$ and $\mathfrak{R}$) and lines ($\mathfrak{s}$ and $\mathfrak{r}$) - adapted from Flídr et al. [31]

boundary layer. Described phenomenon is responsible for the formation of the passage vortex (PV). The existence of more vortices (pressure and suction side corner vortices,) was revealed by the visualization experiments performed by Wang et al. [9]. These vortices interact and unsteady behaviour of the flow has to be expected due to these interactions. The question arises, if this interaction is completely random or if it is periodic.

Secondary flow in the blade cascades was investigated from the unsteady point of view as well. Moore et al. [14] used their previous steady measurements [13] and showed the connection between the dissipation of secondary kinetic energy and deformation work of mean fluid motion operated by turbulent stresses. Zunino et al. [15] and Gregory-Smith et al. [16] found, that the position of the largest total pressure losses matched with regions of high turbulence level. Moreover, Gregory-Smith et al. [16] tried to answer the question posed above and they found one discrete frequency ($f = 32.5$ HZ) in the spectrum which they connected with periodic behaviour of the passage vortex. In the following work, Gregory-Smith et al. [5] performed experiments on cascade with different geometry and they were studying the effects of high inlet turbulence on secondary flow. Frequency characteristics were evaluated in this work as well, but according to the authors, no significant frequency was observed (except one frequency connected with the acoustics). According to the authors' knowledge, these works [5, 16] are the only two, where periodic behaviour of the end-wall flow was investigated in the frequency domain. Another detailed hot-wire anemometry measurements were performed by Perdichizzi et al. [17]. This work among other results showed, that turbulence at the cascade outlet was anisotropic. This anisotropy was gradually transformed into isotropic conditions with increasing distance from the trailing edges of the blades. Papers [5, 15–17] investigated secondary flow under designed conditions with outlet Mach number reaching up to 0.3. Another unsteady investigations were performed by several authors, but most of them were focused on impinging wakes on the blade rows and how they affected the secondary flow e.g. [18, 19].

1.2 Aim of the work

This paper describes an experimental and numerical simulation work focused on an unsteady point of view in an end-wall region of a linear blade nozzle cascade. Unsteady behaviour was expected due to the interaction of vortices in the end-wall region of the cascade. Effects of compressibility (Mach number $M_{2,is}$) and incidence flow angle α_1 were studied for one cascade pitch to chord ratio $t/c = 1$. Different flow parameters were chosen for this study compared to the publications cited above, the lowest Mach number was 0.8 and non-design inlet flow angles were studied as well. Measurements were conducted on the suction surface of the blade in the end-wall region as well as at the blade mid-span, where reference data (for comparison) were acquired.

Another aim of the work was to confirm turbulence anisotropy in the cascade channel mentioned by Perdichizzi et al. [17]. This could help mathematicians to choose a better model of turbulence for their calculations resulting in more accurate data. Isotropic models of turbulence are often used for simulations because calculations are simpler and computational time is shorter. It was, however, shown by Li et al. [20] and by Rumsey et al. [21] that such simplification can cause errors in the obtained data.

Lastly, the in-house numerical code was used to performed simulations and these results were compared with experimental data. Both boundary and initial conditions were set according to the experimental setup.

2 Experimental apparatus, setup and methods

2.1 Apparatus

Experiments were performed in the VZLU laboratory of high speed aerodynamic in a low pressure closed-loop wind tunnel (WT), where Mach number $M_{2,is}$ and Reynolds number $Re_{2,is}$ can be set independently. The working medium in the WT was air. Inlet flow angle α_1 was set by a pair of semi-shaped nozzles placed in front of the cascade. Periodicity of the flow was granted by a large number of blades in the cascade (the cascade contained 9 blades) and thanks to the tailboards placed behind the trailing edges of first and last blade.

Effects were investigated for the nozzle cascade assembled from 9 (pitch to chord ratio $t/c = 1.00$) prismatic blades with chord length $c = 50$ mm, axial chord length $c_{ax} = 36$ and trailing edge thickness $\epsilon = 1$mm.

Unsteady pressure measurements were performed by two pressure transducers EPIH-111-07B glued into the blade. The transducers were glued 0.5 mm under the surface of the blade into the small cavities with a diameter of 0.6 mm. One transducer was positioned at the blade mid-span $z/h = 0.5$ to obtain reference data, while second-one was placed in the near-wall region in position $z/h = 0.04$, see Fig. 2. This place was chosen based on the surface flow visualization, which

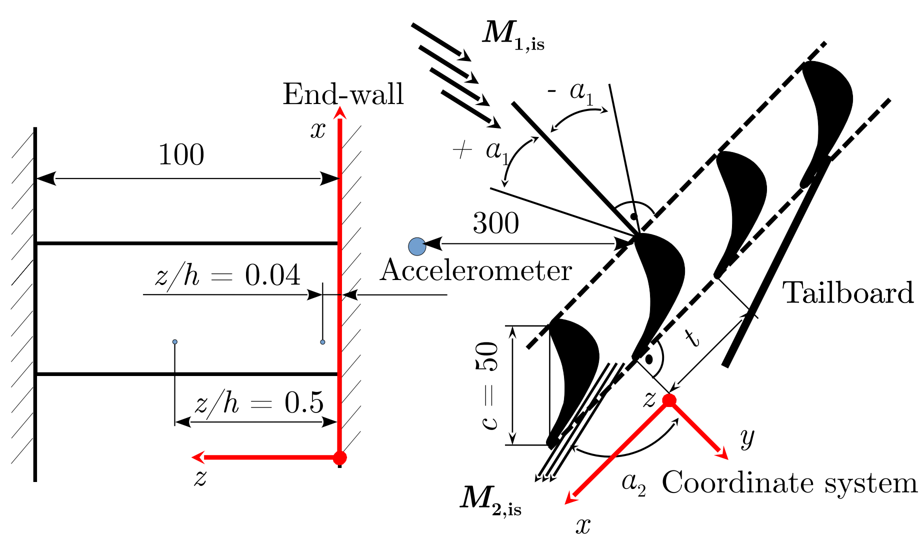

Fig. 2 Cascade geometry—adapted from Flídr et al. [31]

confirmed the expected occurrence of the vortex structures. Unsteady pressure taps were placed on the suction surface of the blade in the position $s/c = 0.71$. Position $s/c = 0.71$ of the pressure taps was chosen with respect to the blade solidity, i.e. that residual material after hole drilling had to withstand the forces acting on the blade.

Steady static pressure measurements at the blade surfaces were performed by means of pressure scanners Scanivalve ZOC33/64PXx2 in one blade channel to obtain Mach number distributions at the blade mid-span in this channel.

2.2 Investigated parameters

Flow regimes were chosen with respect to the operational conditions of the WT and blades (blades were designed for the overloaded high pressure part of the steam turbine). Reynolds number was set constant $Re_{2,is} = 8.5 \times 10^5$. Effects of compressibility $M_{2,is}$ and inlet flow angle α_1 were investigated. Tested parameters are defined in Table 1.

2.3 Methods

2.3.1 Flow regime definition

Flow regimes were set according to the values of both Mach and Reynolds numbers evaluated from the pressure measurement at the cascade outlet. Both similarity criteria were evaluated for the isentropic flow and were defined as:

$$M_{2,is} = \sqrt{\frac{2}{\kappa - 1}\left[\Pi_{201}^{\beta} - 1\right]}, \quad (1)$$

$$Re_{2,is} = \frac{p_2 M_{2,is}\sqrt{\frac{\kappa}{rT_2}}}{\eta_2}, \quad (2)$$

where κ is the ratio of specific heats ($\kappa = 1.4$ for dry air), $\Pi_{201} = p_2/p_{01}$ is the ratio of static and stagnation pressures, p_2 is the static pressure at the cascade outlet, T_2 is thermodynamic temperature at the cascade outlet, $r = 287.12$ J/(kg·K) is the gas constant, $\beta = \frac{\kappa-1}{\kappa}$ is the exponent and η_2 is the dynamic viscosity obtained by Sutherland's formula, see [22].

Table 1 Tested parameters

Case	$M_{2,is}$ (1)	α_1 (°)	Case	$M_{2,is}$ (1)	α_1 (°)
(a)	0.80	20	f)	0.80	20
(b)	0.85	20	g)	0.80	30
(c)	0.90	20	h)	0.80	40
(d)	0.95	20	i)	0.80	50
(e)	1.00	20	j)	0.80	55

2.3.2 Pressure measurement

Measured voltage signals $E(\tau)$ were converted into the pressure $p(\tau)$ by using calibration equations for the pressure transducers. All transducers had approximately linear dependency between pressure and voltage $p = \mathcal{K}E$, where $\mathcal{K}$ is the transducer constant. Pressure signals were transformed into the isentropic velocities by:

$$u_{is}(\tau) = \sqrt{\frac{2\kappa r T_i}{\kappa - 1}\left[\Pi_{01,i}^{\beta} - 1\right]}, \quad (3)$$

where $\Pi_{01,i}$ is pressure ratio, which is defined as:

$$\Pi_{01,i} = \frac{\langle p_{01}\rangle}{p_i(\tau)}, \quad (4)$$

where $\langle p_{01}\rangle$ is the mean value of the reference total pressure measured in front of the WT test section in the relaxation chamber and $p_i(\tau)$ is the time signal measured by the unsteady pressure transducers. These time signals were transformed into the frequency domain by the fast Fourier transformation (FFT). Power spectral density (PSD) was calculated as well as the probability density functions (PDF) and standard deviation (STD) of the signals.

2.3.3 Surface flow visualization

Two solutions of powder dyes (FRONTON inorganic powder dyes for interior and exterior usage) were injected through the taps (∅ 0.6 mm) into the test section. Powder dyes were mixed in a 2% solution of Methylisothiazol for better adhesion of the colours on the surfaces. The volumetric ratio of the dye/solution was 1/8. Orange dye was injected through the taps near the leading edge of the blade (position $s/c \approx 0.1$) at the suction surface. The red dye was injected from the end-wall taps positioned 2.5 cm in front of the cascade into the flow field. Positions of the taps were chosen with respect to the phenomenon under investigation plus on the previous experience discussed by Flídr et al. in [23]. Visualizations were performed for limiting cases a, e and j, respectively, see Table 1.

2.4 Data acquisition and uncertainty

Flow regimes were set in agreement with the steady pressure measurement at the cascade inlet and outlet. Signals were acquired for one second with sampling frequency $f_{sampl.} = 1000$ Hz and with low pass filter $f_{lp} = 100$ Hz. Uncertainty of the measured pressures was 0.1% RDG. Mach number was set with the highest uncertainty of 1% and for Reynolds, number uncertainty was less than 2%.

Steady pressure measurement at the blade surfaces performed by the scanners Scanivalve ZOC33/64PxX2, were measured with an accuracy of 0.08% FS.

Unsteady measurements were performed with sampling frequency $f_{sampl.} = 50$ kHz and with low pass filter $f_{lp} = 10$ kHz. Low pass filter was set according to the expected own frequency of the system ($f_{own} \approx 12$ kHz). Uncertainty of the pressure measured by the transducers EPIH was 0.25% FS. All values of uncertainties were evaluated based on 95% level confidence.

Reference total temperature was measured in the relaxation chamber in front of the test section of the WT by means of Sensorica Humistar HTP-1 hygrometer with the precision of $T = T \pm 0.3$ K.

3 Numerical approach

Calculations were performed using the in-house numerical code based on the solution of the system of averaged Navier-Stokes equations by the finite volumes discretization method. More details were published by Straka in [24, 25]. The system of governing equations was closed with a two-equation turbulence model based on non-linear explicit algebraic relation for the Reynolds stress tensor proposed by Rumsey and Gatski [26, 27]. The turbulence model was complemented with the algebraic model of bypass, separation induced and wall roughness induced boundary layer transition according to Straka and Příhoda [28]. Multiblock structured computational mesh consisted of approximately 1.5×10^6 hexahedral cells. Mesh was clustered toward the wall to ensure that the viscous sublayer was covered with minimal 5 cells ($y^+ < 1$). The inlet boundary layers were evolving on the 800 mm long flat plate in front of the leading edges of the blades to simulate the experimental boundary conditions. The outlet boundary of the computational domain was placed approximately one and half of the blade-chord behind the trailing edge. The total temperature 300 K, the total pressure, the inlet flow angle α_1, the turbulence intensity 2.25%, and the turbulent to molecular viscosity ratio 80 were prescribed as the inlet boundary conditions. The averaged value of the static pressure across one blade-pitch was prescribed at the outlet boundary. Values of both total inlet and static outlet pressures correspond with given Reynolds and Mach numbers.

4 Results and discussion

4.1 Mid-span Mach number distribution

Figure 3 shows distributions of Mach number at the blade mid-span obtained from the steady pressure measurement. Position $s/c = 0.71$ of the unsteady pressure taps is highlighted by the dashed line in the graphs. Dash-dot lines represent data obtained from the numerical simulations. Regime defined by $\alpha_1 = 55°$ and $M_{2,is} = 0.8$ was not numerically investigated, therefore this data line is not present in the Fig. 3a.

Surface Mach number distributions were nearly unaffected by the variation of the flow regime defined by isentropic Mach number $M_{2,is}$ in the region behind the leading edge of the blade on the suction side of the blade (approx. up to $s/c = 0.25$). Significant changes can be observed from $s/c \approx 0.4$, as is evident in Fig. 3a, where blade loading increased rapidly with increasing Mach number $M_{2,is}$. Shock wave formed in the region close to the unsteady pressure taps, when Mach number was $M_{2,is}$=0.95 and 1, as can be seen from Fig. 3a. The position of the shock wave was not fixed, but oscillated in some range of s/c as will be discussed below. Deviations between measured and calculated data were within 10% of experimental data. The exception was observed in the region around the stagnation point, where the deviation increased (for explanation

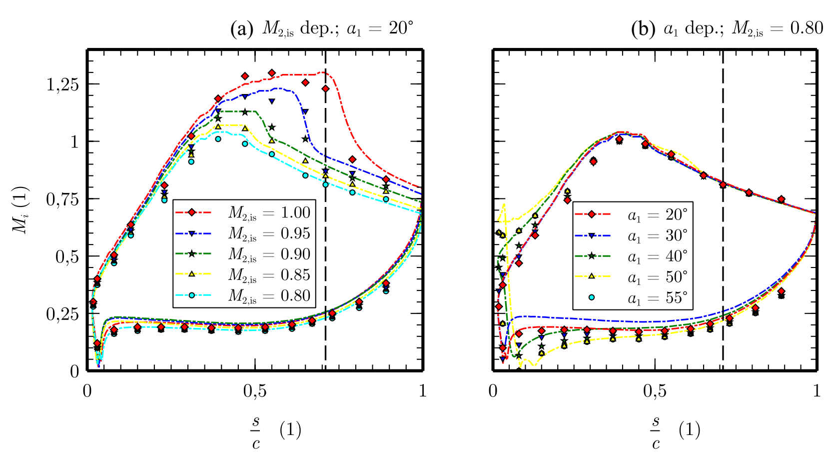

Fig. 3 Blade Mach number distributions at the mid-span, comparison of experimental data (points) and numerical simulation (dash-dot lines), colours of data **a** Mach number dependencies and **b** inlet flow angle development

see below). Note, that higher deviations were observed on the pressure side of the blade.

Variation of the incidence flow angle α_1 affected Mach number distributions near the leading edge of the blade due to the movement of the stagnation point on the surface. A small separation region behind the leading edge of the blade on the suction surface formed when the inlet flow angle was increased to $\alpha_1 = 50°$. This separation region was not affected by a further increase of α_1, as demonstrates Fig. 3b. Blade loading was similar in the area where the unsteady pressure taps were localized ($s/c = 0.71$), note, that in the end-wall region situation could be different due to the complexity of the flow field. Deviations were more significant compared to the situation, where the compressibility effect was investigated. In this case, deviations reached up to 20% depending on the α_1. Higher deviations were observed in the region near the stagnation point due to the lowest velocities in this region. These deviations were calculated as a difference between the experimental and numerical data in the corresponding point *s*/*c*.

4.2 Surface flow visualization compared with numerical simulations

Suction surface flow visualization is depicted in Fig. 4, where positions of the unsteady pressure taps are highlighted together with separation lines $\mathfrak{S}_{2,s}$ and $\mathfrak{S}_4$. Pressure tap in the near-wall region was positioned in the place, where the secondary flow occurred, as is evident from the visualizations. Results of the numerical simulations in terms of limiting streamlines on the suction surface, the pressure surface and the end-walls are depicted in the figure as well.

Vortices were localized in the near-wall region reaching $z/h = 0.12$ in the case of nominal incidence angle $\alpha_1 = 20°$ and $M_{2,is} = 0.80$, it demonstrates Fig. 4a. These structures rapidly enlarged (reached up to $z/h \approx 0.22$) as the inlet flow angle increased from $\alpha_1 = 20°$ to $\alpha_1 = 55°$, see Fig. 4a and b. These findings agree well with the theory of secondary flow introduced by Hawthorne [29]. When Mach number was increased up to 0.90, the shock wave formed and strengthen, when Mach number increased further up to 1. It was observed that the shock wave was oscillating in range of $s/c \in (0.65; 0.75)$, see Fig. 4c. Complicated flow structures raised up in the region, where the secondary flow and the shock wave interacted. Nevertheless, the near-wall flow was not affected by the shock wave, as can be seen from the figure. All results obtained from the 3D numerical simulation agree well with presented surface flow visualizations, as is shown in Fig. 4. Vortical structures reached up to $z/h = 0.10$ for $\alpha_1 = 20°$ and $M_{2,is} = 0.80$, up to $z/h = 0.20$ for $\alpha_1 = 50°$ and $M_{2,is} = 0.80$ and $z/h = 0.17$ for $\alpha_1 = 20°$ and $M_{2,is} = 1.00$ on the suction surface of the blade. Interaction of vortical structures in the end-wall region with shock wave is clearly visible in the case of flow regime $\alpha_1 = 20°$ and $M_{2,is} = 1.00$ from numerical simulation. The saddle point in front of the leading edge moved into the blade channel and more upstream, when the $\alpha_1$increased. The position of the saddle point was not significantly affected by the increase of Mach number. In the region where the shock wave interacted with the vortical structures, however, the recirculation region formed. The same behaviour was observed in the case of pressure surface, i.e. with the increase α_1, vortical structures were enlarged. In the case of $\alpha_1 = 20°$ they reached up to $z/h = 0.015$ meanwhile for $\alpha_1 = 50°$ up to $z/h = 0.033$. Insignificant evolution with the change of Mach number was detected.

4.3 Unsteady measurement

Unsteady behaviour was investigated based on the evaluation of power spectral density (PSD), probability distribution function (PDF) and standard deviation (STD) of the measured signals.

4.3.1 Power spectral density

In Fig. 5 evolution of PSDs with variation of Mach number $M_{2,is}$ (first column) and incidence flow angle α_1 (second column) are depicted. Spectra obtained in the end-wall region were approximated by the function of f^{δ}, where δ was varying exponent. Frequencies up to 25 Hz were filtered out due to their connection with the regulation of the WT and therefore were not interesting for the studied phenomena.

PSD at the blade mid-span was significantly affected by the variation of $M_{2,is}$. According to the profile design and tested flow regimes, transition of the boundary layer to the turbulence was expected in the region near the leading edge of the blade, i.e. the flow was expected turbulent in the area, where the unsteady pressure measurements were performed. Results obtained from the experiments at the blade mid-span suggest, that fully developed turbulence was reached in the case of $M_{2,is} = 0.95$ and 1.00, where the slope of the PSD $f^{-5/3}$ was found at the blade mid-span, see Figs. 5d and 6e. The frequency of the oscillation of the shock wave, mentioned above, was detected in Fig. 5e, and was approximately 1000 Hz (peak in the graph). Damping of the dominant frequencies can be observed with increasing Mach number at the blade mid-span. It was probably caused by interaction with the shock wave.

PSD in the near-wall region was nearly unaffected by the variation of Mach number and it was independent of the changes at the blade mid span. It is evident from Fig. 4, that flow structures in the end-wall region and at

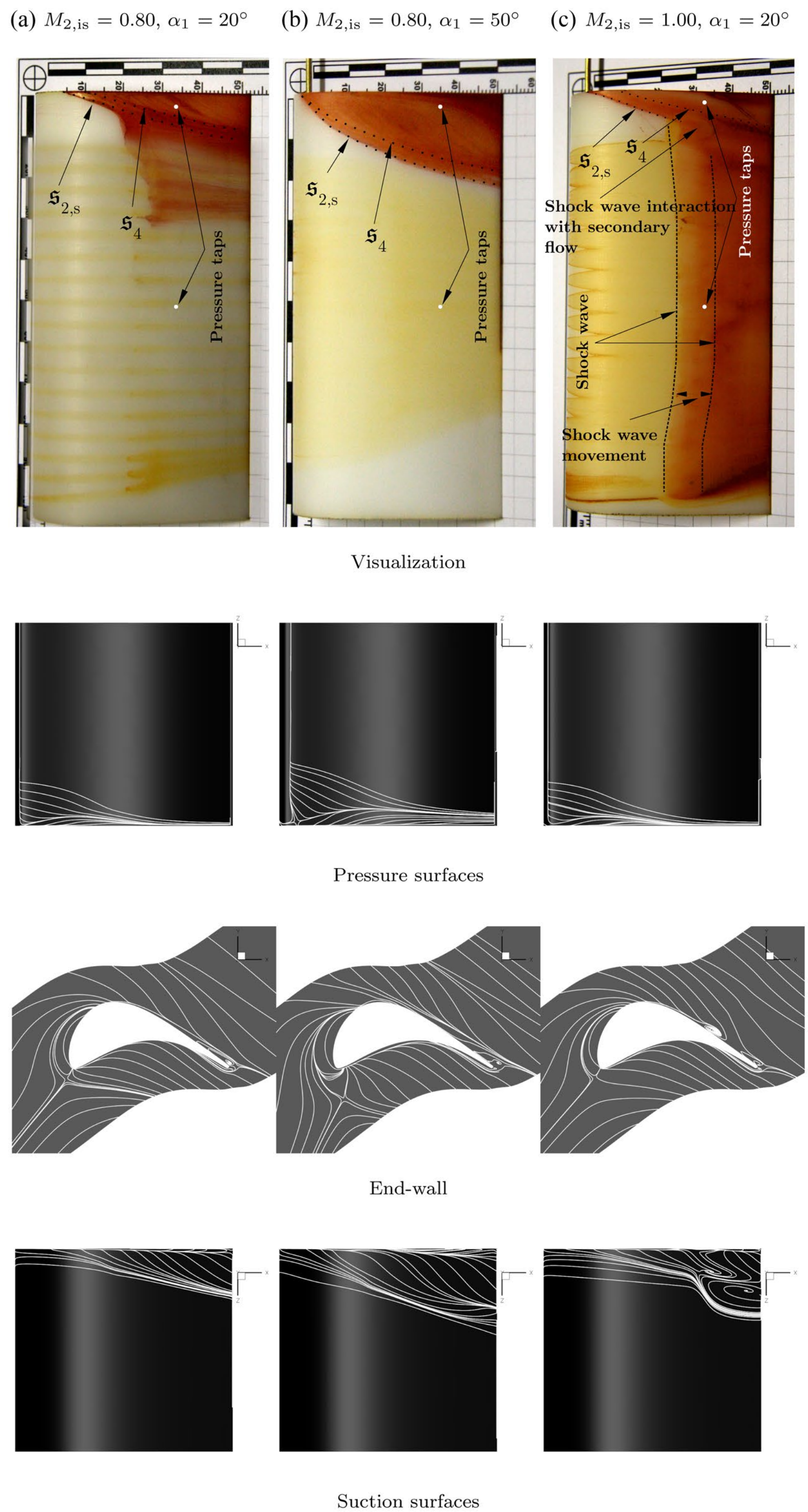

Fig. 4 Surface flow visualization compared with numerical simulations

the blade mid-span were different in nature (separation line $\mathfrak{s}_4$ divided the flow field into two parts). These findings can be traced as well in Flídr et al. [23], where the visualization study was more complex. In the near-wall region, three significant frequencies ($f \approx 1200, 1400$ and 2500 Hz) were detected. These frequencies remind the same throughout the measurement, but their magnitude rose with increasing studied parameter. This periodic behaviour may have been connected with the interactions between the vortices occupying the near-wall region. Comparison

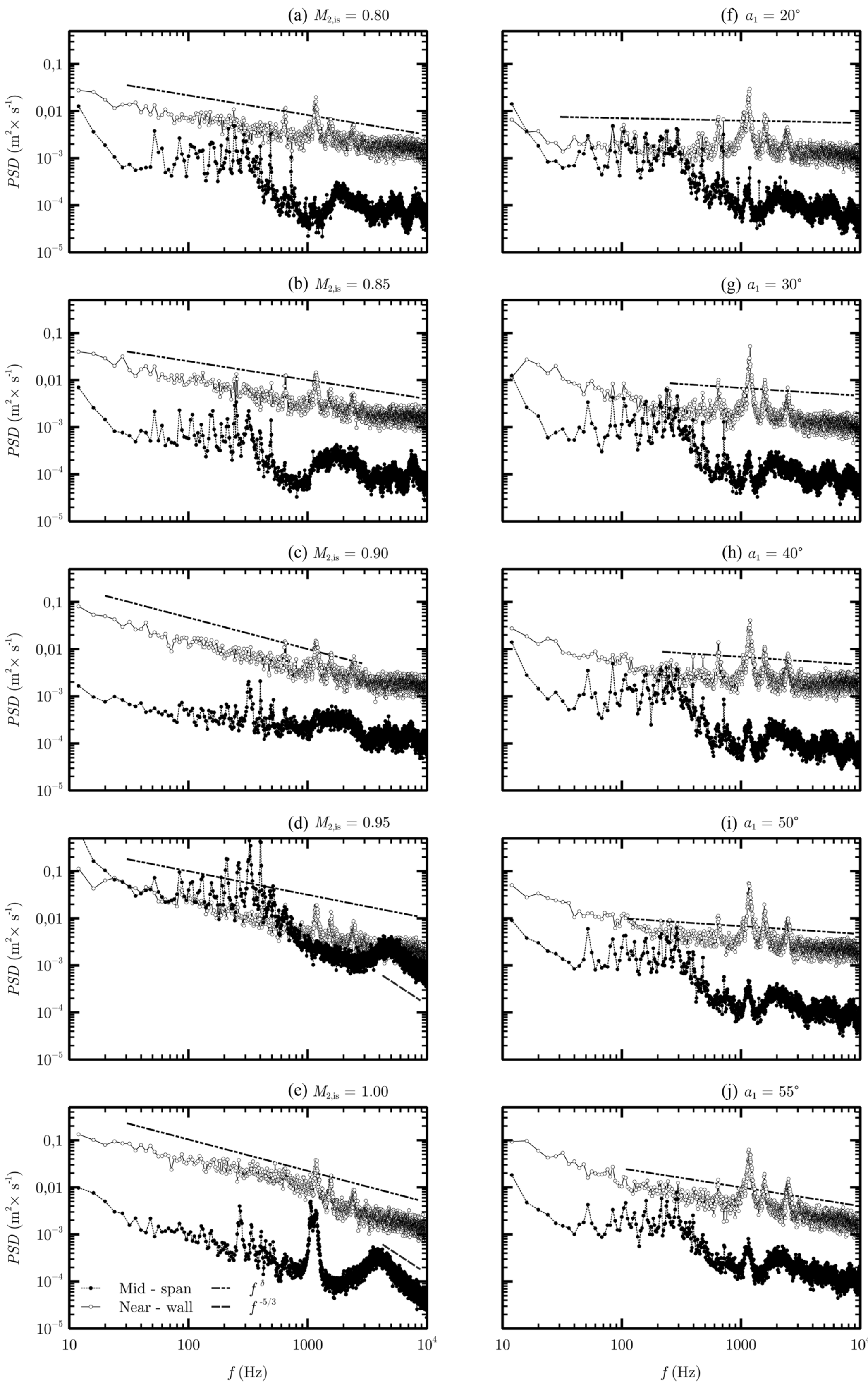

Fig. 5 Power spectral density

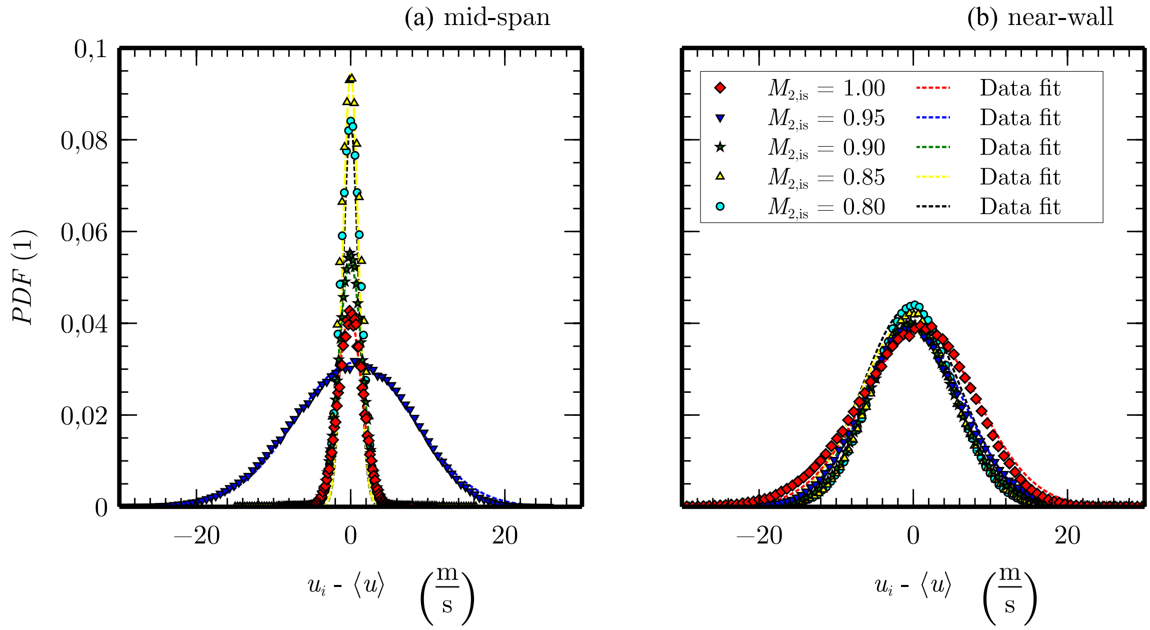

Fig. 6 Probability distribution functions for different Mach numbers $M_{2,is}$ **a** blade mid-span, **b** near-wall region

of data obtained here with the findings of Gregory-Smith et al. [16] showed that there is a huge difference between the spectra. Gregory-Smith et al. [16] presented a diagram, where only one significant frequency in the end-wall region was detected. Moreover, its value was significantly lower compared to this study. It can be caused by the different flow conditions, because works [5, 14, 16] were conducted with outlet Mach numbers around 0.1. Higher outlet Mach number ($M_{2,is}$ =0.3) was investigated by [17], but it does not reach even half the value presented in this paper.

Spectra in the end-wall region contained more energy compared to the blade mid-span, as demonstrated in data shown in Fig. 5. The exception was found for the case of Mach number $M_{2,is}$=0.95 (Fig. 5d), where the mid-span spectrum was affected by the shock wave oscillating across the unsteady pressure tap (it can be seen from visualization in Fig. 4).

The energy was more uniformly distributed in the near-wall region and could be approximated more accurately in the mentioned form of power function f^{δ}.

Generally, exponent δ was decreasing with increasing studied parameter. Its value was $\delta = -0.002/6$ for nominal regime. It dropped to a value of $\delta = -4.5/6$ in the case of $M_{2,is}$ =1.00 and $\delta = -2.5/6$ in the case of α_1 55°, respectively. This result suggests, that the turbulence was more developed in the cases of *e)* ($M_{2,is}$ = 1, α_1 = 20°) and *j)* ($M_{2,is}$ = 0.80, α_1 = 55°) compared to the flow conditions *a)* and *f)* ($M_{2,is}$ = 0.8, α_1 = 20°). With increasing investigated criterion spectra contained more energy.

4.3.2 Probability density function and its approximation

Many works deal with the turbulence and its statistics, see e.g. Lesieur [30]. The question was raised, whether the distribution of velocity fluctuation is Gaussian or not. It is connected with the conditions of the central limit theorem and whether they are fulfilled. The flow was turbulent in the presented study, therefore probability density functions of the signals were analysed as well to contribute to the topic. Probability density functions evolution with Mach number are shown in Fig. 6 and with inlet flow angle in Fig. 7. According to the data, PDFs were symmetric with respect to the mean values of the velocity, therefore were approximated by the distributions in the form of:

$$PDF = \frac{1}{b\sqrt{2\pi}} e^{-\frac{1}{2}\left(\frac{u_i}{a}\right)^2} \tag{5}$$

with a and b as variables. If σ^2 denotes variance of the signal and relation $a = b = \sigma$ holds, then PDF was normally distributed.

This relationship was not found in the case of the present study. Variation from normal distribution is demonstrated in graphs Fig. 8, where ratios of a/b are plotted as functions of Mach number (Fig. 8a) and inlet flow angle (Fig. 8b), respectively. It is evident, that with increasing Mach number and inlet flow angle, approximation of the PDF in the end-wall region converges to normal distribution. At the blade mid-span, no such statement can be made.

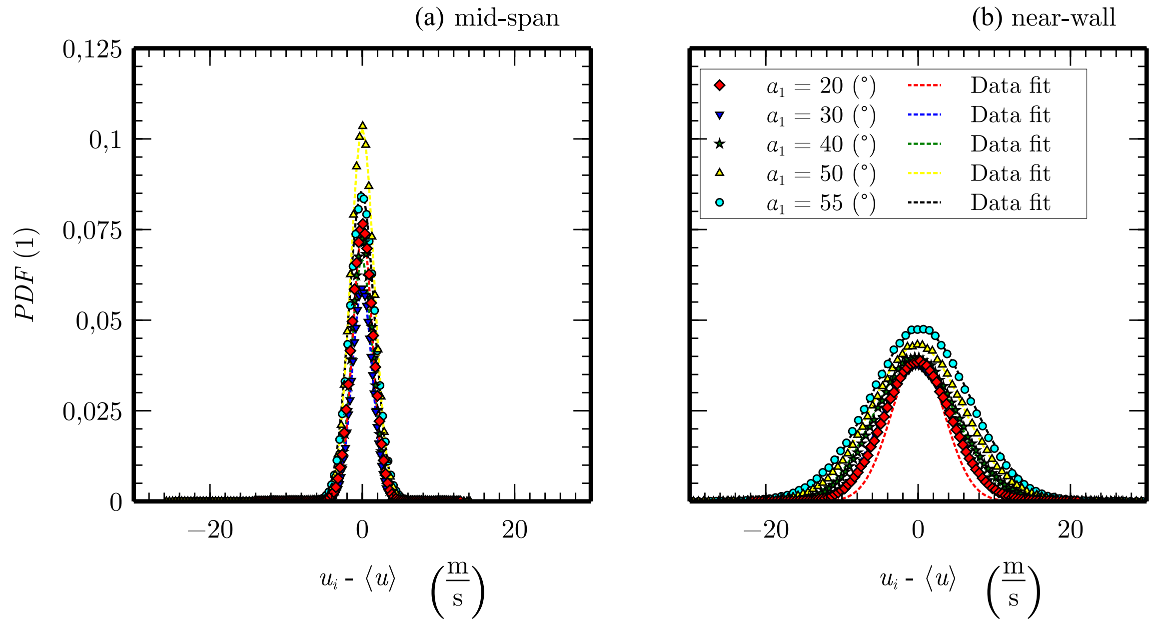

Fig. 7 Probability distribution functions for different inlet flow angles α_1 **a** blade mid-span, **b** near-wall region

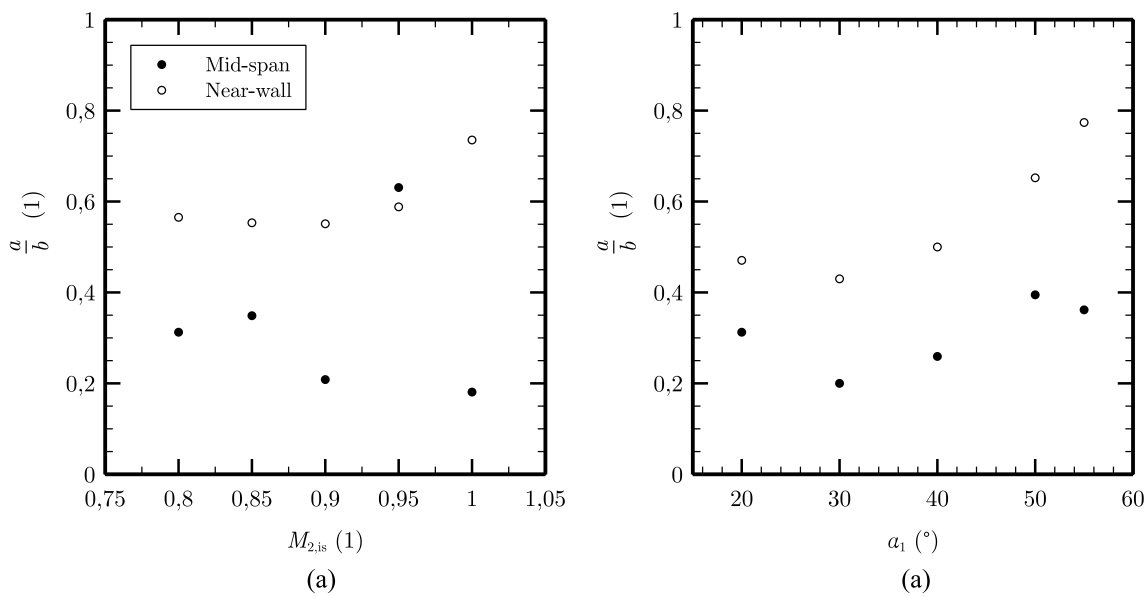

Fig. 8 Ratio of parameters *a* and *b* as a function of **a** Mach number, **b** inlet flow angle

4.3.3 Integral values

Ratios of the isentropic velocities $\mathcal{U} = \frac{u_{nw}}{u_{ms}}$ in the end-wall region and at the blade mid-span as well as ratios of their STDs $\mathcal{U}_{STD} = \frac{(u_{nw})_{STD}}{(u_{ms})_{STD}}$ are shown in Fig. 9a (Mach number dependency), and Fig. 9b (inlet flow angle effect).

Ratio $\mathcal{U}$ decreased from 0.8 to 0.5 with increasing Mach number. Ratio $\mathcal{U}_{STD}$ demonstrated, that with increasing $M_{2,is}$, fluctuations were approximately four times larger in the end-wall region compared to the mid-span except for the case of $M_{2,is} = 0.95$ when the shock wave was moving across the pressure tap. This phenomenon enhanced the

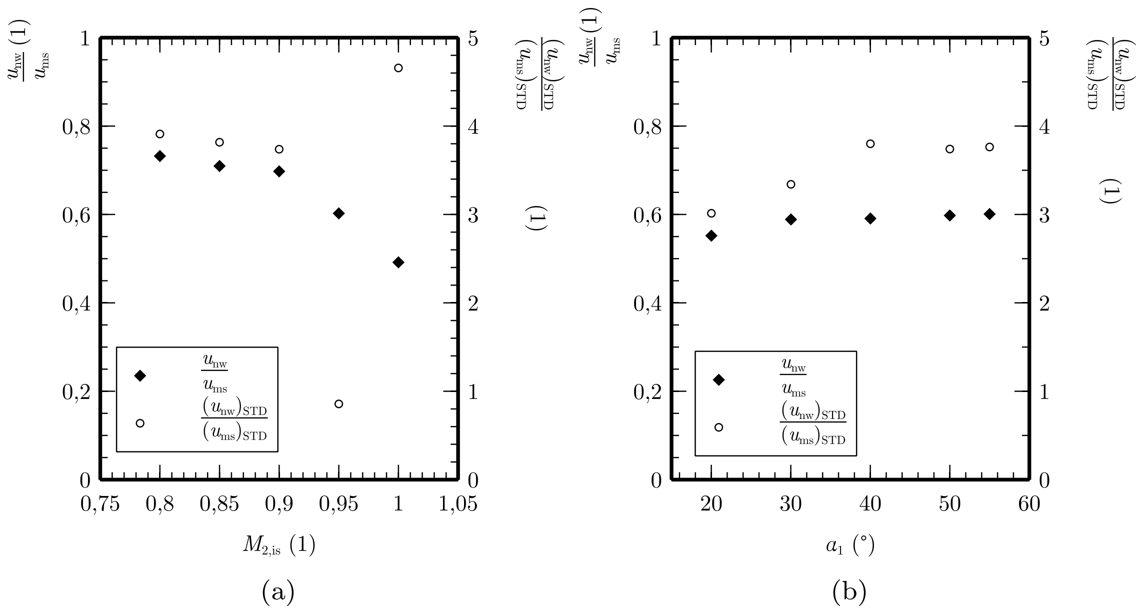

Fig. 9 Ratios of unsteady velocities and their STDs **a** Mach number effect, **b** inlet flow angle effect

fluctuations at the blade mid-span and they were comparable in magnitude.

Inlet flow angle did not affect the ratio of velocities $\mathcal{U}$ significantly, as demonstrates Fig. 9b. Fluctuations in the end-wall region were magnified with increasing inlet flow angle. It was caused by the stronger secondary flow in the near-wall region. These results were already presented by Flídr et al. [31], where STDs were evaluated in terms of normalized pressure signals. Ratio $\mathcal{U}_{STD}$ was rising up until $\alpha_1 = 40°$. From that value stayed approximately constant, i.e., that the fluctuations in both regions were rising in the same manner. Magnification of the fluctuation at the blade mid-span for overloaded regimes was caused by the enlargement of the separation region behind the leading edge of the blade.

5 Conclusion

Unsteady behaviour of the flow in the linear blade cascade was investigated by means of pressure measurement in the end-wall region as well as at the blade mid-span. Unsteady measurements were supplemented by flow visualization and steady pressure measurements. Effects of compressibility and inlet flow angle were studied. Obtained data imply that:

- Interaction between the shock wave and end-wall flows was observed for the highest Mach number, therefore complicated flow structures raised. This phenomenon should be investigated in the future in much more detail. Mid-span flow and end-wall flow can be, on the other hand, considered independent of each other if this shock wave was not formed.
- Anisotropic turbulence was observed in the cascade, so the observation of Perdichizzi et al. [17] was confirmed. This result can be helpful to the CFD community when deciding which turbulence model to choose for their calculations in similar cases.
- Energy contained in the spectra increased with increasing Mach number, moreover, the slope of the spectra -5/3 was found from $f = 4$ kHz at the blade mid-span, when the shock wave form. With increasing studied parameters ($M_{2,is}$ and α_1) slope of the spectra in the end-wall region decreased. It means, that turbulence was developing from the anisotropic to the isotropic, but this development remains unfinished.
- Analysis of power spectra shows three significant frequencies in the near-wall region. This periodic behaviour was related to the interaction of vortices that occupied this place.
- PDFs and their analysis showed, that distributions studied here were probably not Gaussian.
- Fluctuations were in all cases a few times higher in the end-wall region compared to the mid-span except the case, when the shock wave oscillated across the pressure tap.
- Results obtained from flow visualization and numerical simulations (limiting streamlines on the surfaces) were in good agreement. Mach number distributions were simulated with quantified deviations. Presented data showed that the used in-house model can simulate and

predict the experimental results in a studied case with accuracy described in the paper.

Hot-Wire anemometry will be used in the future for the detailed measurements at the cascade outlet to support some of the conclusions. Regimes investigated in the future will be reduced based on the data presented here.

Acknowledgements The work was realized within project No. TN01000007 National Centre for Energy. The project is co-financed by the government support of the Technology Agency of the Czech Republic within the program of National Centres of Competency.

Declarations

Conflict of interest The authors declare that they have no conflict of interest.

References

1. Hodson HP, Dominy RG (1987b) The off-design performance of a low-pressure turbine cascade. ASME J Turbomach 109:201–209
2. Perdichizzi A, Dossena V (1993) Incidence angle and pitch-chord effects on secondary flows downstream of a turbine cascade. ASME J Turbomach 115:1–8
3. Perdichizzi A (1990) Mach number effects on secondary flow downstream of a turbine cascade. ASME J Turbomach 112:643–651
4. Hodson HP, Dominy RG (1987) Three-dimensional flow in a low-pressure turbine cascade at its design conditions. ASME J Turbomach 109:177–185
5. Gregory-Smith DG, Cleak JGE (1992) Secondary flow measurements in a turbine cascade with high inlet turbulence. J Turbomach 114:173–183
6. Jilek J (1986) An experimental investigation of the three-dimensional flow within large scale turbine cascades, ASME paper no. 86-GT-170
7. Chen LD, Dixon SL (1986) Growth of secondary flow losses downstream of a turbine blade cascade. ASME J Turbomach 108:270–276
8. Langston LS (1980) Crossflow in a Turbine cascade passage. ASME J Eng Power 102:866–874
9. Wang HP, Olson SJ, Goldstein RJ, Eckert ERG (1997) Flow visualization in a linear turbine cascade of high performance turbine blades. ASME J Turbomach 119:1–8
10. Sieverding CH (1985) Recent progress in understanding of basic aspects of secondary flow in turbine blade passage. ASME J Turbomach 107:248–257
11. Langston LS (2000) Secondary flow in axial turbines—a review. In: International symposium on heat transfer in gas turbine systems
12. Ligrani P, Potts G, Fatemi A (2017) Endwall aerodynamics loss from Turbine. Components within gas turbine engines. Propulsion Power Res 6:383–391
13. Moore J, Adhye RY (1985) Secondary flows and losses downstream of a turbine cascade. J Eng Gas Turbines Power 107:961–968
14. Moore J, Shaffer DM, Moore JG (1987) Reynolds stress and dissipation mechanism downstream of a turbine cascade. J Turbomach 109:258–267
15. Zunino P, Ubaldi M, Satta A (1987) Measurement of secondary flow and turbulence in a turbine cascade passage, ASME Paper No. 87-GT-132
16. Gregory-Smith DG, Walsh JA, Graves CP, Fulton KP (1988) Turbulence measurements and secondary flow in a turbine rotor cascade. J Turbomach 110:479–485
17. Perdichizzi A, Ubaldi M, Zunino P (1992) Reynolds stress distribution downstream of a turbine cascade. Exp Thermal Fluid Sci 5:338–350
18. Ciorciari R, Kirik I, Niehuis R (2014) Effects of unsteady wakes on the secondary flows in the linear T106 Turbine Cascade. J Turbomach, vol 136
19. Sinkwitz M, Winhart B, Engelmann D, di Mare F, Mailach R (2017) Experimental and numerical investigation of secondary flow structures in an anular lpt cascade under periodical wake impact—part 1: experimental results. In: International symposium on transport phenomena and dynamics of rotating machinery, Maui Hawaii
20. Li W, Yang L, Ren J, Jiang H (2014) Algebraic anisotropic eddy viscosity model for separated flows of internal cooling channels, ASME Paper no. GT2014- 25591
21. Rumsey ChZ, Gatsky TB (2000) Morrison, turbulence model prediction of a strongly curved flow in a u-duct. AIAA J 38:1394–1402
22. Shuterland W (1893) The viscosity of the gases and molecular force. Philosophical Magazine Series 5 36:507–531
23. Flídr E, Jelínek T, Kladrubský M (2019) Visualization study of the secondary flow within a linear blade cascade, Topical Problems of Fluid Mechanics conf. proc., pp 72–81
24. Straka P (2015) Numerical simulation of high-swirl flow in axial turbine stage. Exp Fluid Mech Conf Proc, pp 752–759
25. Straka P (2016) Modelling of unsteady secondary vortices generated behind the radial gap of the axial turbine blade wheel, ECCOMAS Congress Conf Proc
26. Rumsey CL, Gatski TB (2001) Recent turbulence model advances applied to multielement airfoil computations. J Aircraft 38(5):904–910
27. Rumsey CL, Gatski TB (2003) Summary of EASM turbulence models in CFL3D with validation test cases. Report - (**NASA/TM-2003-212431**)
28. Straka P, Příhoda J (2016) Extension of the algebraic transition model for the wall roughness effect. EPJ Web Conf 114:02114
29. Hawthorne WR (1951) Secondary circulation in fluid flow. Proc Roy Soc Ser A 206:374–387
30. Lesieur M (2008) Turbulence in fluids. Springer, The Netherlands
31. Flídr E, Kladrubský M, Jelínek T, (2020) Unsteady pressure measurement in an end-wall region of a linear blade cascade, topical problems of fluid mechanics conf proc